Applied Catalysis B: Environmental 323 (2023) 122166

Contents lists available at ScienceDirect

Applied Catalysis B: Environmental

journal homepage: www.elsevier.com/locate/apcatb

On factors of ions in seawater for CO_2 reduction

Shengjie Bai [1], Mengmeng Song [1], Tengfei Ma, Feng Wang, Ya Liu *, Liejin Guo *

International Research Center for Renewable Energy, State Key Laboratory of Multiphase Flow, Xi'an Jiaotong University, Xi'an, Shaanxi 710049, China

ARTICLE INFO

Keywords:
CO_2 reduction
Seawater
Electrolyte
Copper
Chemical fuel

ABSTRACT

Performing solar-driven CO_2 reduction reaction (CO_2RR) on the sea is desirable for future renewable energy landscape. However, CO_2RR cannot be directly operated in natural seawater due to the unsuitable ionic environment. Herein, we studied CO_2RR from the perspective of ions in seawater electrolyte on Copper. We find that multi-ions mixture in seawater could accelerate CO_2RR by tuning electrode, local pH, and bulk electrolyte simultaneously. Specially, Na^+_K^+ mixture has a workable buffer capacity for regulating local pH and activating CO_2 within electric-double-layer. Cl^-_Br^- mixture induces microstructural and actively changes on Cu electrode. While, in anions-mixture, SO_4^{2-} would lower overpotential by reducing polarization loss in bulk electrolyte. Under this hierarchical structure of multi-ions in local environment, a well-performed CO_2RR is achieved after optimizing ions-concentration and anode catalysts. Finally, by coupling a gas diffusion electrode with optimized seawater, the photovoltaic-driven electrolyzer obtained a 9.88 % solar-to-fuel efficiency (6.15 % solar-to- carbon-based fuels) under direct sunlight.

1. Introduction

CO_2 reduction reaction (CO_2RR), as a potential path toward reusing CO_2 to produce fuel, is of great significance for alleviating the shortage of fossil fuels and combatting global climate change. The photo-electrochemical CO_2RR is a potentially effective approach to recycling greenhouse CO_2 and providing fuel for energy storage simultaneously [1–5]. However, most of the present research was conducted in fresh water with a single species of solute [6]. In actual production and application, the ultrapure water-based electrolyte is very precious [7]. To achieve the strategic research goals in the field of energy and environment, it is necessary to explore workable solutions for CO_2RR in earth-abundant water resources (such as seawater, sewage).

In fact, according to previous studies, natural seawater has many viable values as electrolyte [8–10]. Numerous ions in seawater can be directly applied as the supporting electrolyte [9–12]. Also, seawater is considered an enrichment sink for anthropogenic CO_2, which meets the concentration requirements of the reaction. Although seawater has been reported to support hydrogen generation *via* water splitting [7,13,14], it has rarely been involved in CO_2RR so far. Nakata et al. demonstrated the electrochemical CO_2RR on the Boron-doped diamond electrode in natural simulated seawater based on NaCl solution at ambient conditions, which produces HCOOH with high yields [15]. Lee and Wallace tested the electrocatalytic CO_2RR in seawater using a nano-porous Ag electrode. They found that Ca^{2+} in the seawater could form calcium carbonate and be deposited on the electrode, thereby reducing the electrochemically active sites [16]. Xiang and coworkers indicated a proof-of-concept involving a bipolar membrane electrodialysis cell and a vapor-fed CO_2RR cell [17]. Despite the simultaneous capture and conversion of CO_2 from seawater being achieved, additional power input and expensive equipment are still inevitable.

To date, the interaction mechanism of various ions in seawater-based electrolytes is still unclear for CO_2RR. However, we think that it is insufficient to simply use NaCl aqueous solution as the simulated seawater. Previous studies did illustrate that ions have a significant influence on CO_2RR [18,19]. ATR-FTIR absorption spectrum was used by Sartin et al. to expose that cations play an important role in adsorption/reduction of *CO [20].

Singh et al. reported that larger cations have lower *pKa* of cation hydrolysis to serve as buffering agents, which leads to higher local CO_2 concentration and promotes CO_2RR [21]. Meenesh et al. found that the local electric field could be weakened by several additional anions, which increases the energy loss of the cell [22]. Verma et al. discovered that the bond formed between the adsorbed anion and C in the CO_2 molecule benefitted the electron transfer from the adsorbed anions to CO_2, thus initiating the conversion of CO_2 [23]. Gao et al. explored that

* Corresponding authors.
E-mail addresses: yaliu0112@mail.xjtu.edu.cn (Y. Liu), lj-guo@mail.xjtu.edu.cn (L. Guo).
[1] Authors made equal contributions.

https://doi.org/10.1016/j.apcatb.2022.122166
Received 22 August 2022; Received in revised form 19 October 2022; Accepted 9 November 2022
Available online 11 November 2022
0926-3373/© 2022 Elsevier B.V. All rights reserved.

the overpotential reduced and the current density increased in the order of Cl^-, Br^-, and I^- [19]. So far, the investigation of the actual parameters of seawater is rarely involved in current literature. It is necessary to carry out comprehensive research on electrochemical CO_2RR within natural seawater.

In this study, the influence of the ions in natural seawater was systematically studied for CO_2RR on Cu, an economic catalyst for producing C_{2+} species [24,25], aiming to reveal the feasibility of CO_2RR in seawater-based electrolytes. The reaction path and energy barriers were also calculated *via* density functional theory (DFT) to study rate-limiting steps and stabilization of the key intermediates for CO_2RR. The gas bubble adhesion test and electrode surface property characterization were conducted to clarify the influence mechanism of seawater-based ions and their mixtures on electro-catalytic CO_2RR. Moreover, a hierarchical multi-ions application mechanism in seawater was detailly discussed, and a seawater pretreatment strategy, which changes the composition and concentration of natural seawater, was proposed for CO_2RR. A photovoltaic (PV) –driven CO_2RR under the optimized seawater-based electrolyte was conducted on a gas diffusion electrode (GDE) and a 9.88 % solar-to-fuel efficiency was obtained. We have preliminarily explored the direct application of seawater-based electrolytes in CO_2RR.

2. Experimental methods

2.1. Preparation of the electrolytes

The electrolytes involved are shown in Table S1. The involved ions include the majority of ionic species in natural seawater. The method of removing the Ca^{2+} and Mg^{2+} is conducting a two-electrode chronopotentiometry reaction with a copper cathode (2 × 3 cm) under −5 mA/cm^2. During the galvanostatic reaction, the cathode was mechanically polished per cycle (1 h).

2.2. Cu plate electrodes and GDE

The processing method was in the Supporting Information. Commercially available Cu plates (99.9999 %) purchased from Alfa Aesar were cut into 1.5 cm^2 strips. The Cu plates were polished with 1200 mesh emery paper for 1.5 min and then electro-polished in phosphoric acid (GR, 85 wt%) at 2 V *vs.* counter electrode (Cu) for 2 min. After mechanical and electrochemical polishing, the Cu plates were cleaned with ultra-pure water and dried under the N_2 atmosphere for use.

The GDEs were prepared by spraying catalyst ink onto carbon paper (Sigracet 29 BCE) with a carrier gas of nitrogen at 65 °C on a heater (IKA). The Cu NPs ink consists of 35 mL isopropanol, 548 μL Nafion (Fuel Cell, D520, Alcohol based 1000 EW, 5 wt%), and 105 mg Cu NPs (Kejing H.F., particle diameter ≤ 40 nm). Before use, the ink was sonicated to disperse it homogeneously. The amount of Cu NPs was controlled at 400 μg/cm^2 on the carbon paper.

2.3. Electrochemical measurements

A typical H-type reactor consisted of two half-reaction compartments separated by an anion exchange membrane (Selemion AMV, AGC Inc.). The reaction area of the anode and cathode is 1 cm^2. 2 mL of electrolyte was added to each half-reaction chamber. The CO_2 (99.999 %) was continuously bubbled into the reactor by using a gas mass flow controller (Alicate) with a flow rate of 5 sccm. The outlet gas flow rates were monitored by a flow meter (Alicate). All electrochemical measurements were performed with an Autolab potentiostat (PGSTAT302N). A leek free Ag/AgCl electrode (3 M KCl, 1 mm OD, 100 mm barrel length,) was used as the reference electrode. A Pt foil was used as the counter electrode under three-electrode operation, while for full cell operation we used NiFe LDH to reduce the overpotential for oxygen evolution reaction. The NiFe LDH used in this study was synthesized following documented procedures [26]. Electrochemical active surface area (ECSA) was determined in the same three-electrode configuration. Electrochemical impedance spectroscopy (EIS) was performed at frequencies ranging from 100 kHz to 1 Hz with a potential perturbation of 10 mV. All potentials were converted into a reversible hydrogen electrode (RHE) scale through Eq. 1. The potential for a 3.5 M KCI Ag/AgCl electrode is 0.21 V. During the electrochemical testing, *Ru* (uncompensated resistance) was 80 % compensated *via* the current interrupt method.

$$E\ (vs\cdot\ \mathrm{RHE}) = E\ (vs\cdot\ \mathrm{Ag/AgCl}) + 0.21\ \mathrm{V} + 0.0591\ \mathrm{V} \times \mathrm{pH} \quad (1)$$

2.4. PV-GDE integration and measurements

The single-crystalline Si solar modules were supplied by LONGi Co., Ltd. The illuminated surface area of each unit Si module was 1.5 cm^2 (12 cm^2 total of 8 modules with series-connected), and the catalyst electrode areas (geometric) were 1 cm^2 each. The *j–V* characteristics of series-connected Si solar cells under natural solar irradiation (532 W/m^2) were measured using the same Autolab potentiostat (PGSTAT302N) with a two-electrode configuration at *c.a.* 1:00 PM. The conversion efficiency (η_{pv}) of the PV cells was calculated as Eq. (2):

$$\eta_{pv} = I_{sc} \times V_{oc} / P \times A \quad (2)$$

where I_{sc}, V_{oc}, P, and A are short-circuit current (A), open-circuit voltage (V), illumination intensity (W•m^{-2}), and illuminated area (m^2).

The eight series-connected Si cell was combined with a GDE electrolyzer. The optimized seawater (pH=6.3) after CO_2-saturated was circulated in the anode and cathode chambers with a constant flow rate of 2 mL/min. The CO_2 was continuously bubbled into cathode chambers at a flow rate of 15 sccm. The i–t and V–t data of the cell under irradiation were acquired by the above-mentioned electrochemical workstation. The illumination intensities (P) and air temperatures were recorded every 20 min by a PC–2–T1 solar radiation monitoring system (Jin Zhou Sunshine Meteorological Technology Co., Ltd., Jinzhou, Liaoning, China. Spectral range: 280–3000 nm).

3. Results and discussion

3.1. CO_2RR in natural seawater

Before performing CO_2RR in the natural seawater, the insoluble species were removed *via* preliminary filtration. Next, a chronoamperometry was employed in the natural seawater with Cu as the cathode. However, CO_2RR is blocked after 4 h' testing, as shown in Fig. 1a. The Faraday efficiency (FE) of the CO_2RR product is less than 5 % (Fig. S1a–b), and the current density at −1.3 V *versus* reversible hydrogen electrode (*vs.* RHE) is only −5 mA/cm^2 (Fig. S1c–d). Moreover, there are lots of visible insoluble species on the electrode surface, as shown in Fig. 1b. Initially, the Cu foil surface is smooth and shiny. After 4 h' CO_2RR in natural seawater, lots of insoluble substances are visible to the naked eye appears. The images of energy dispersive spectroscopy (EDS) mapping reveal that these insoluble contains Mg or Ca, which is also confirmed by inductively coupled plasma mass spectrometry (ICP–MS) (Figs. S2–S3) and crystallographic analysis (Fig. S4a). Since these insoluble species covered the surface of the electrode, the electric double-layer structure near the electrode was disruptive, and even the Impedance is increased (Fig. S4b). It hindered the transport of ions, reduced the mass transfer efficiency of the reactants, and thus blocked CO_2RR. In comparison, H_2 evolution reaction (HER) in individual Ca^{2+} and Mg^{2+} electrolyte is predominant, and current density in individual Ca^{2+} electrolyte sharply drops earlier than in Mg^{2+} electrolyte, which indicates Ca^{2+} is easier to deposit on the

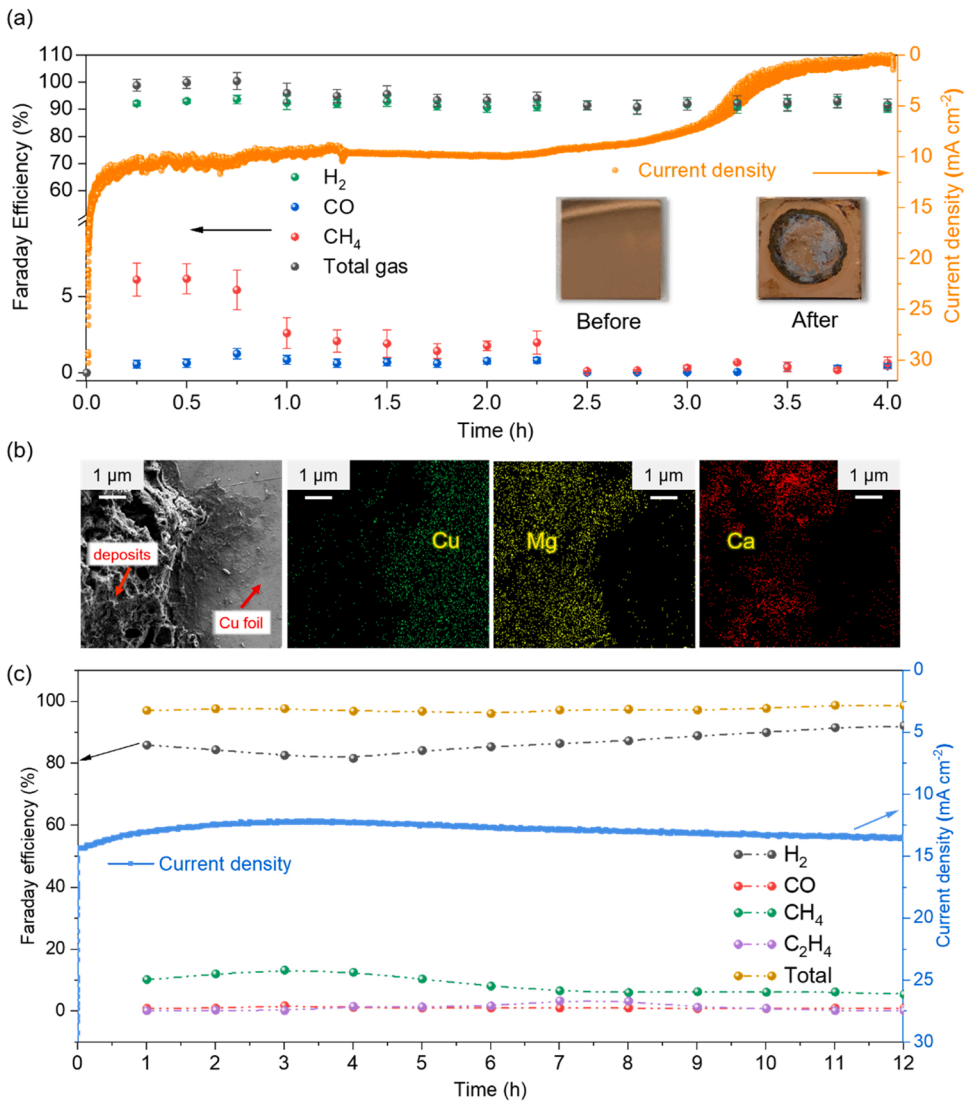

Fig. 1. CO_2RR in natural seawater. (a) The 4 h' stability test of CO_2RR in natural seawater on pure Cu electrode. The CO_2RR was carried out at an applied potential of −1.15 V *vs.* RHE. Error bars represent the mean ± standard deviation of at least 3 individual experiments. The insert photographs refer to the Cu electrode surface before and after the 4 h′ CO_2RR. (b) EDS mapping images of the pure Cu electrode after the 4 h′ CO_2RR. (c) The 12 h′ i–t curve and CO_2RR performance of seawater after electrochemical removal of Ca^{2+} and Mg^{2+}.

electrode surface than Mg^{2+} (Fig. S5). Also, as shown in the LSV curve after 3 h CO_2RR in Fig. S6, the potential at 10 mA cm^{-2} in individual Ca^{2+} electrolyte is more positive than that in Mg^{2+} individual electrolyte. Due to the solubility product (*Ksp*) of $CaCO_3$ (2.8 ×10^{-9}) being smaller than that of $MgCO_3$ (3.5 ×10^{-8}), Ca^{2+} preferentially forms $CaCO_3$ precipitation on the electrode surface in the electrolyte continuously bubbling CO_2. Therefore, the suppression of the CO_2RR by Ca^{2+} is more obvious than that of Mg^{2+}. However, in the CO_2RR of the natural seawater (Fig. S7), since the ion concentration is positively correlated with the precipitation reaction, the potential change is correlated with the change of the Mg^{2+} with a higher concentration. To eliminate their interference, Ca^{2+} and Mg^{2+} should be removed in subsequent research and applications of seawater-based CO_2RR.

After removing the Ca^{2+} and Mg^{2+} by an electrical electrochemical method (see experiment section), we found that the residual Ca^{2+} and Mg^{2+} in the electrolyte (100 mL) would not disturb the i–t curve after 12 cycles (Figs. S7–S9). The concentration of Ca^{2+} and Mg^{2+} in the electrolyte was 8.2 × 10^{-5} mol L^{-1} and 7.3 × 10^{-5} mol L^{-1} respectively (Table S1, marked optimized 1), which is practically negligible (Figs. S7–S9). As shown in Fig. 1c, although the faraday efficiency of CO_2RR products is quite low (*c.a.* 10 %), the current density can be very stable (Fig. 1c), which means the obstruction from Ca^{2+} and Mg^{2+} was almost eliminated.

3.2. Individual cation or anion in the electrolytes

Given the CO_2RR selectivity was still low (less than 20 %) in the seawater-based electrolytes after removing Ca^{2+} and Mg^{2+}, we present a more in-depth discussion on each cation or anion within the seawater and their impacts on CO_2RR.

Except for the removed Ca^{2+} and Mg^{2+}, Na^+ and K^+ are the major cations in natural seawater [27]. Here, 0.1 M Na^+ and K^+ bicarbonate solutions were tested individually to explore how cations affect the CO_2RR in electrolytes. From Figs. 2 and S10, CO_2RR performance in K^+ bicarbonate solution has a higher current density, lower HER, and more hydrocarbons, especially C2+ (Fig. S11). Several previous works have demonstrated that the hydrated K^+ with a larger radius has a vaster buffering capacity and facilitates the stabilization of intermediates by electrostatic interactions with dipolar intermediates [21,28–30]. DFT analysis shows that adsorbed K^+ on the surface can lower the free energy for CH_4 and C_2H_4 formation (Fig. S12a–b).

To explore the role of individual anions in CO_2RR, 0.1 M Cl^-, Br^- and SO_4^{2-} sodium solutions were employed as electrolytes for the CO_2RR. As shown in Fig. 2, the selectivity of hydrocarbons in three individual anion electrolytes is in the order: Br^->Cl^->SO_4^{2-}, especially C2+ (Fig. S13). We noted that this order is consistent with the solvation ability order of three anions on the metal electrode (Br^->Cl^->SO_4^{2-}) [31–36]. According to previous studies, the strong solvated anions formed a direct chemical

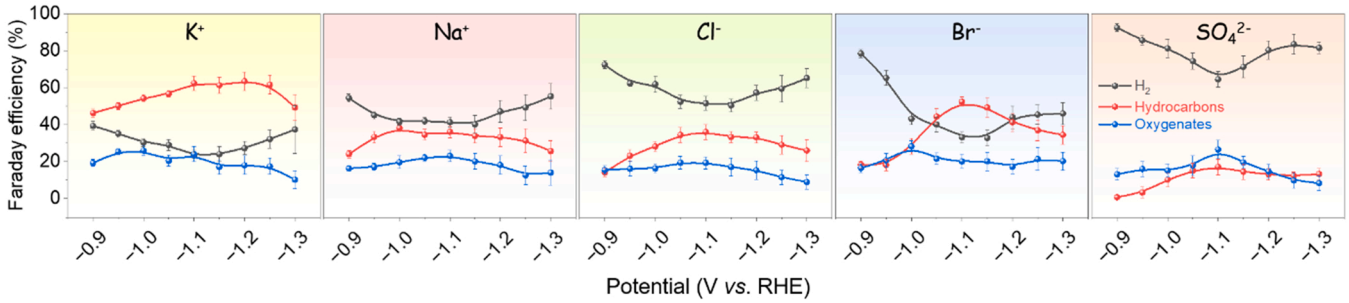

Fig. 2. Potential-dependent FE of CO_2RR by Cu electrode in individual ion electrolytes ($K^+/Na^+/Cl^-/Br^-/SO_4^{2-}$). Hydrocarbons include Methane, Ethylene, and Ethane. Oxygenates include Formate, Acetic acid, Methanol, Ethanol, Acetaldehyde, Ethylene glycol, Hydroxyacetone, n-Propanol, and Propionic acid. The solid lines with spheres indicate the trends of FE. Error bars represent the mean ± standard deviation of at least 3 individual experiments.

bond with Cu, and this specific adsorption was considered to be beneficial for both thermodynamic and kinetic CO_2RR, particularly C–C coupling [19,37]. Also, we examined the electrochemical behavior in the individual anion electrolytes (Figs. S14–S15). The Br^- and Cl^- electrolytes do present higher current densities and overpotential than SO_4^{2-} one in most cases.

Notably, the SO_4^{2-} does lower the overpotential (Fig. S15) and gets a higher half-reaction energy conversion efficiency (ECE, see Supplemental information for the detailed Equation and Table S2) than the other two (Fig. S13a). We consider that the SO_4^{2-} with high ionic strength and activity coefficient could reduce ohmic polarization, which results in a more negative applied potential (Fig. S15) [38,39]. The EIS results shown in Fig. S16 validated this conjecture.

Besides, the changes in the Cu surface morphology from different anions in the electrolyte are also in the order: $Br^->Cl^->SO_4^{2-}$ (Fig. S17), which is also beneficial for the selectivity of C2+. This agrees with previous literature [19,40]. DFT calculations about these three anions were further performed to kinetically confirm the effect of these individual ions. (Fig. S18), Br^- has lower ΔG than the other two for *COOH generation from activated CO_2. Moreover, Cl^- and Br^- in the electrolyte have both inherent stronger specific adsorption and a lower energy barrier than SO_4^{2-} for *COOH formation and stabilization [19,20], so they show better CO_2RR performance, especially in producing C2+. For SO_4^{2-}, there is a high uphill barrier in the formation of *COOH, which causes the CO_2RR to proceed with difficulty. Despite the lower overpotential in the SO_4^{2-} electrolyte than the other two anions (Fig. S14), it

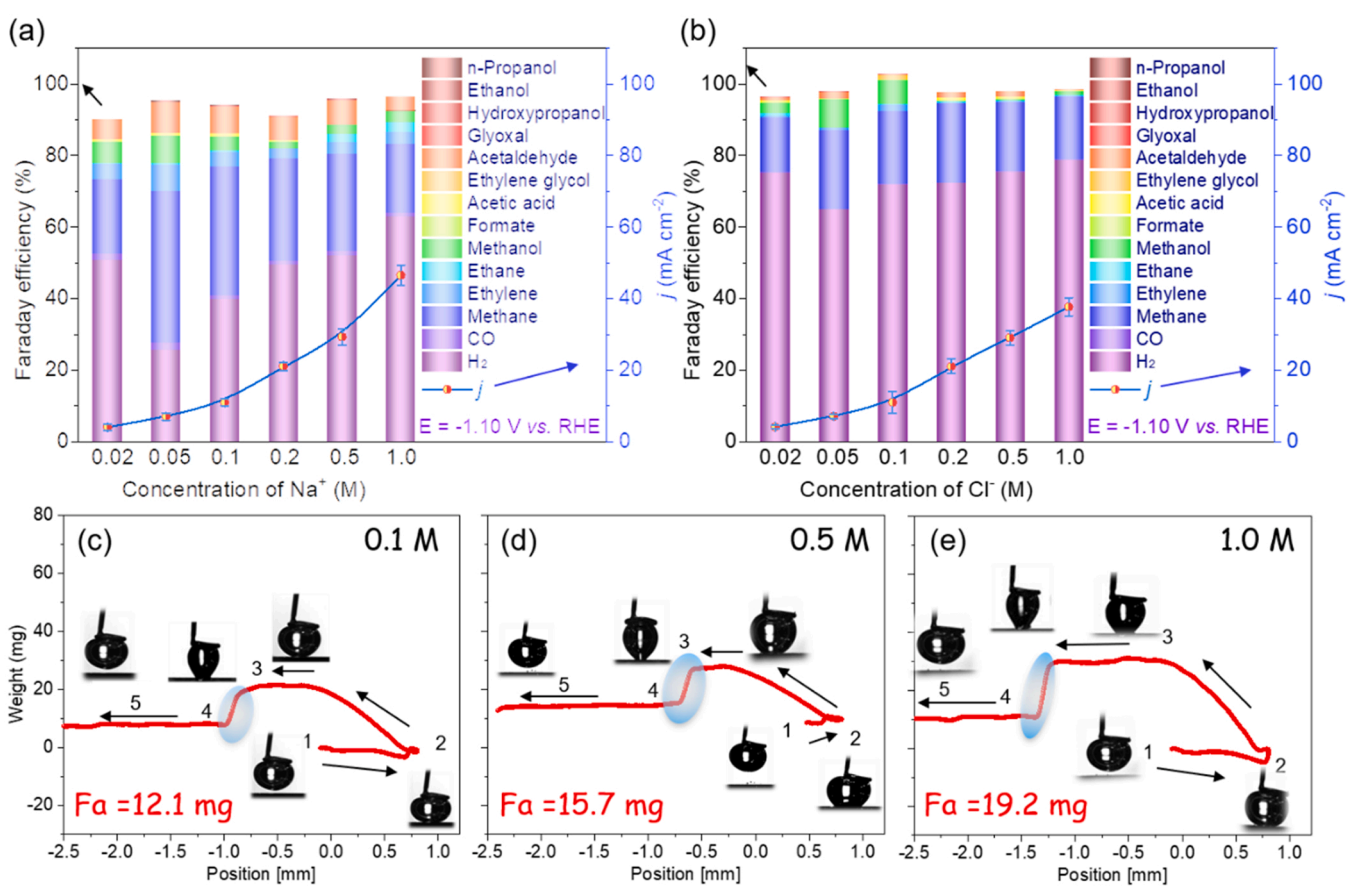

Fig. 3. The effect of ion concentration on CO_2RR performance and CO_2 Adhesion Ability. (a and b) Distribution of CO_2RR products at different Na^+ and Cl^- concentrations. The CO_2RR was executed at an applied potential of −1.10 V *vs.* RHE. The solid line with a red dot indicates the current density change trend at different concentrations. Error bars represent the mean ± standard deviation of at least 3 individual experiments. (c, d, and e) The CO_2 gas bubble adhesive force measurements of Cu electrode in 0.1 M, 0.5 M, and 1.0 M $NaHCO_3$ electrolytes saturated by CO_2. The Fa refers to the bubble adhesive force to the electrode interface.

is attributed to the promotion of HER rather than CO_2 conversion (Figs. 2 and S13). Besides, the roles of individual ions were investigated in Fig. S19. The current densities and selectivities could maintain stability for 4.5 h.

3.3. The concentration of the ions

High salinity of seawater is also an important factor affecting CO_2RR. To get more insights into the concentration of electrolyte, we carried out the CO_2RR in different concentrations at potentials of −1.10 V *vs.* RHE, which was the optimal potential for CO_2RR in $NaHCO_3$ solution. Since Na^+ and Cl^- are the major cation and anion in natural seawater [27], a

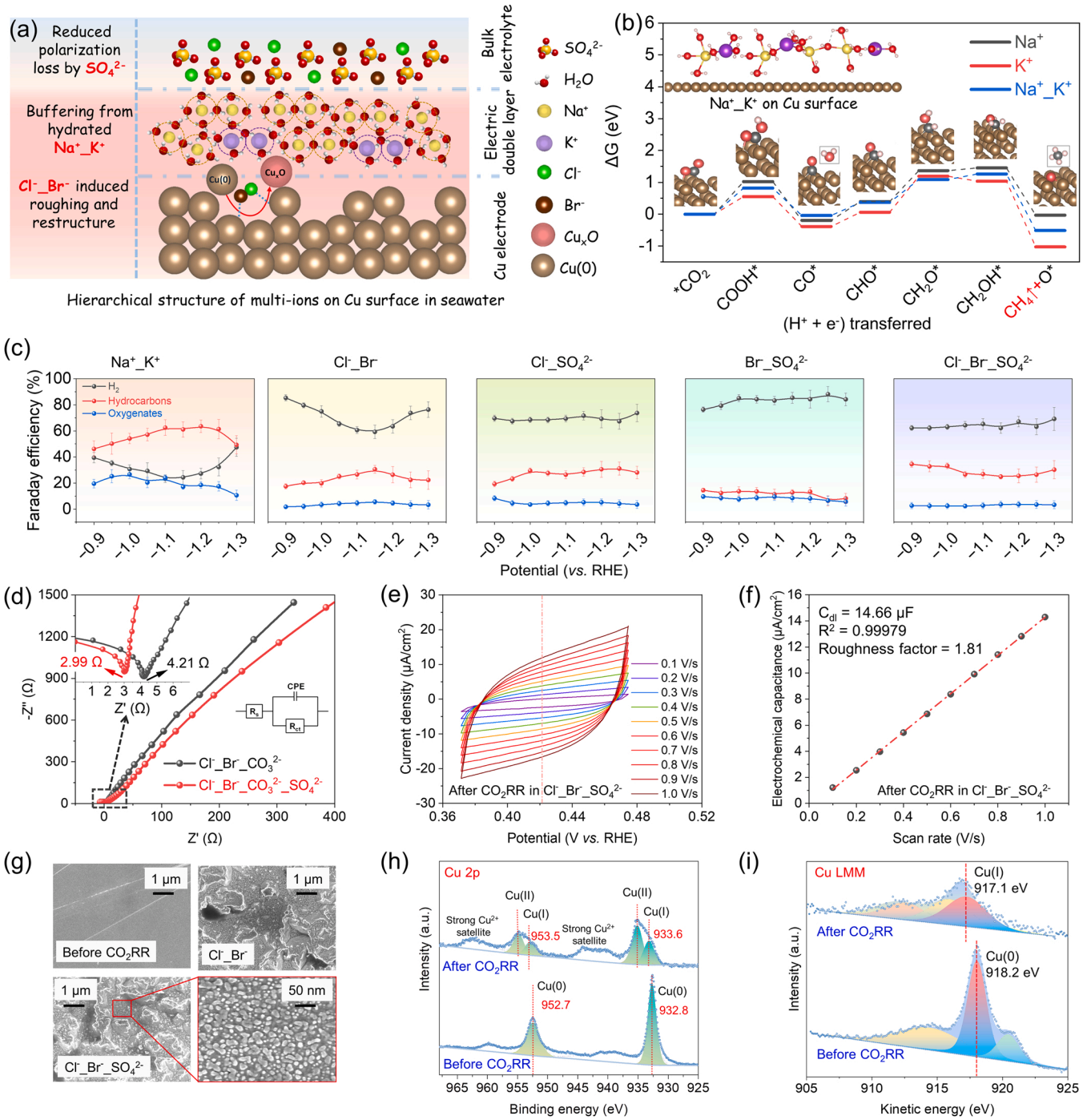

Fig. 4. A hierarchical application in multi-ions mixed electrolytes based on seawater. (a) Schematic illustration of hierarchical application. (b) Energetics diagrams for the lowest energy pathways to CH_4 on pure Cu surface in Na^+, K^+, and Na^+_K^+ electrolytes. The insert indicates the model of Na^+_K^+ couplings on the Cu surface. (c) FE of CO_2RR at different applied potentials by Cu electrode in Na^+_K^+, Cl^-_Br^-, Cl^-_SO_4^{2-}, Br^-_SO_4^{2-} and Cl^-_Br^-_SO_4^{2-} five anions mixed electrolytes. (d) Nyquist plots of Cu electrode in the Cl^-_Br^-_CO_3^{2-} and Cl^-_Br^-_CO_3^{2-}_SO_4^{2-} electrolytes. (e) Cyclic voltammetry at the range of 0.37–0.47 V (*vs.* RHE) under different scanning rates in the Cl^-_Br^-_SO_4^{2-} mixed electrolyte. (f) Plot of capacitive current densities of pure Cu electrode *vs.* scanning rate. (g) The change of surface morphology of Cu electrode by Cl^-_Br^- and Cl^-_Br^-_SO_4^{2-} mixed electrolytes. (h and i) Cu 2p XPS and Cu Auger spectra of Cu electrode before and after 1 h's CO_2RR in Cl^-_Br^-_SO_4^{2-} mixed electrolyte.

series of $NaHCO_3$ and NaCl aqueous solutions (0.05 M, 0.1 M, 0.2 M, 0.5 M, 0.8 M, and 1 M) were used as the electrolyte for CO_2RR, as shown in Table S1.

From Figs. 3a and b, when the concentration is very low, *ca.* 0.02 M, HER in both cations and anions electrolyte is predominant. Conversely, excessive electrolyte concentration is also unfavorable for CO_2RR. When Na^+ concentration exceeds 1 M, a current density exceeding 40 mA/cm^2 is obtained, but the selectivity of the carbon hydroxide is decreased. For the effect of electrolyte concentration on CO_2RR, two aspects should be concerned. Firstly, high electrolyte concentration brings about high conductivity, thereby presenting a higher current density (Figs. 3a, b, and S20). However, a high concentration of non-buffer anions (*i.e.* Cl^-) would reduce solubility and diffusion of the CO_2. Therefore, the reaction tended to produce H_2 because the CO_2 near the interface of the electrode is not replenished. Secondly, ion concentration is closely related to the buffering agents in the electrolyte. The buffer capacity of CO_3^{2-}/HCO_3^- would increase as the concentration of $NaHCO_3$ decreases [41,42]. The increased HCO_3^- could promote the mass transfer of the continuously replenished CO_2 *via* rapid equilibrium with the CO_3^{2-} [43,44]. A high concentration of non-buffer anions resulted in a lower buffer capacity and increased polarization loss (Fig. S16) [18,45]. When the cation concentration is higher than 1 M, except for the effect of steric hindrance and excessive non-buffer anions [46–48], the adhesion force (see supplemental experimental procedures) of CO_2 bubbles on the electrode surface is enhanced (Figs. 3c–e), resulting in a poor mass transfer. Therefore, compared to the natural seawater (Na^+: 0.48 M, Cl^-: 0.52 M), the suitable electrolyte concentration range of Na^+ or Cl^- for CO_2RR is 0.05 – 0.3 M.

3.4. A hierarchical application in multi-ions mixed electrolytes

As an ion sink, multiple ions in seawater exist in a mixture [49]. Thus, individual anion and cation solution cannot reflect the intrinsic electrolyte environment in seawater-based CO_2RR. To gain deeper insight into the underlying mechanism of multiple ionic environments in seawater on CO_2RR, multiple ion-coupling environments of natural seawater concentration equivalents are used for CO_2RR test.

To this end, we proposed a mechanism for the hierarchical application of multiple seawater-based ions couplings on the CO_2RR (Fig. 4a). In detail, (1) Cl^- and Br^- can specifically be adsorbed on the Cu surface and reconstructed the surface, which mainly acts on the electrode side; (2) The Na^+_K^+ cations–coupling served as the regulators for stabilizing the local CO_2 by buffering interfacial pH, which primarily worked at the outer Helmholtz plane (OHP); (3) For SO_4^{2-}, the nature of high ionic strength and activity coefficient could reduce ohmic polarization losses from the bulk electrolyte.

For further validation, we conducted CO_2RR in multi–ions mixed electrolytes. Given that the nature of Ca^{2+} and Mg^{2+} would block the CO_2RR, they were no longer mentioned here. A bicarbonate aqueous solution of Na^+_K^+ served as a cations mixed electrolyte. Compared with individual Na^+, K^+ electrolytes, Na^+_K^+ mixed electrolyte has a weaker suppression of HER (Fig. S21a) and higher half-reaction ECE at −1.2 V *vs.* RHE (Fig. S21b), whereas the surface of the pure Cu electrode does not change obviously before and after the reaction (Figs. S22–S23). To interpret the observation, we analyze the buffer capacity by comparing the p*K*a of Na^+, K^+, and Na^+_K^+ mixed electrolyte (Table S3) near the Cu electrode [21,30]. The Na^+_K^+ mixed electrolyte has a mediocre p*K*a of 9.114 and better buffer capacity than individual Na^+. To kinetically investigate the reaction pathway on the Cu surface in the seawater cations electrolyte, we compared the energy barrier of each step during CO_2RR in Figs. 4b and S21. The model of Na^+_K^+ coupling on the Cu electrode was shown in Figs. 4b and S22. CH_4 and C_2H_4 formation in Na^+_K^+ mixed electrolytes are comparable to those in individual cations. As such, it is practicable to use Na^+_K^+ as the supporting electrolyte and buffer for seawater-based electrolyte in CO_2RR, whereas the poorer HER suppression (Figs. 4c and S21) is caused by higher concentration.

For mixed anions, the sodium salt solutions of Cl^-_Br^-, Cl^-_SO_4^{2-}, Br^-_SO_4^{2-}, and Cl^-_Br^-_SO_4^{2-} were employed as the anions mixed electrolyte (Table S1). As shown in Fig. 4c, in the Cl^-_Br^- mixed system, H_2 selectivity is less than 70 % from –1.05 to −1.20 V *vs.* RHE. Within the range of –0.90 to −1.15 V *vs.* RHE, the CO_2RR performance in the Cl^-_Br^- system strongly depends on the potential change. When Cl^- and Br^- existed simultaneously in the electrolyte, specific competitive adsorption occurs on the electrode surface [50]. The specific competitive adsorption had been verified to be potential-dependent and beneficial to CO_2RR [51,52]. While the potential is more negative, the CO_2RR is gradually suppressed.

DFT calculation shows that the Cl^-_SO_4^{2-} and Br^-_SO_4^{2-} hold sharply high uphill barriers toward the formation of *COOH (from activated CO_2) and *CHO (from *CO), and are less stable in intermediates (Fig. S24). Thus, poor HER suppression is obtained in the Cl^-_SO_4^{2-} and Br^-_SO_4^{2-} systems. Also, the SO_4^{2-} could reduce the resistance of the mixed anions electrolytes, which causes a lower overpotential (Figs. 4d, S25, S26–S27).

In the Cl^-_Br^-_SO_4^{2-} mixed electrolyte, the selectivity of H_2 is less than 70 % and hydrocarbon exceeds 20 % within the measured potential range, which is the most dramatic of the four mixed electrolyte systems. Meanwhile, the formation of multi-carbon products is preferred in the Cl^-_Br^-_SO_4^{2-} system (Fig. S28). By observing the electrode surface properties before and after CO_2RR (Figs. 4e–4g and S29–S30), we discovered that the Cu electrode changed notably after CO_2RR. Except for the roughening, a large number of nano-grooves appear on the surface of the pure Cu electrode (Fig. 4 g), so that the original electric double layer on the Cu electrode surface is changed (Fig. S31) and a larger electrochemical geometric area is obtained (ECSA, Figs. 4e, f and S32, Table S4). Compared with the pure Cu electrode (before CO_2RR), the roughness factor on the Cu electrode after CO_2RR in Cl^-_Br^-_SO_4^{2-} mixed electrolyte was 1.81 (Table S4). Besides, the simulation results indicate that the potential distribution of electrolytes on a rough electrode surface is disordered and the current density would be higher than on a smooth surface (Fig. S31b). The micro-heterogeneity of electrode surfaces also varies the interfacial pH gradients and increases OH^- formation [41,53].

To provide more information about the surface electronic states and chemical composition of Cu electrode during the CO_2RR in the Cl^-_Br^-_SO_4^{2-} mixed electrolyte, we performed X-ray photoelectron spectroscopy (XPS, in Fig. 4 h) and X-ray diffractometry (XRD, in Fig. S30) analysis on Cu foil before and after CO_2RR. Before CO_2RR, peaks of the Cu $2p_{1/2}$ (952.7 eV) and Cu $2p_{3/2}$ (932.8 eV) belonged to the Cu(0) signal. After 1 hs CO_2RR, peaks attributed to Cu^+ (933.6 eV and 953.5 eV) and Cu^{2+} (935.0 eV and 954.9 eV) emerged [54,55]. The Cu 2p XPS spectrum indicates the presence of Cu(0), Cu(I), and Cu(II) species after CO_2RR, but the peaks associated with Cu(I) and Cu(II) in the spectra before CO_2RR are absent, suggesting the formation of multiple states Cu after 1 h′s CO_2RR. Fig. 4i shows Cu LMM Auger spectra acquired from the Cu foil after 1 h′s CO_2RR. It is further confirmed that Cu(I) was derived from the effects of adsorbed anions, especially the Cl^- with higher concentration, which underwent a corrosion reaction and partial oxidation with the surface-activated Cu [56,57]. As shown in the spectra of Cu foil after CO_2RR in the Cl^-_Br^-_SO_4^{2-} mixed electrolyte (Fig. S30), diffraction peaks at about 29°, 36°, 42°, 61°, and 73° are indexed to the (110), (111), (200), (220) and (311) planes of Cu_2O nanocrystals (JCPDS NP.05–667) respectively. Previous research had verified that the presence of multiple states of Cu during CO_2RR could promote the selectivity of hydrocarbons and oxygenates [58,59]. This is why CO_2RR in the Cl^-_Br^-_SO_4^{2-} mixed electrolyte exhibited better performance. ICP–MS analysis (Fig. S33) further supports that the electrode surface was more corroded under the Cl^-_Br^-_SO_4^{2-} mixed system than in others.

Additionally, for Cl^-_Br^-_SO_4^{2-} mixture, the rate-limiting step of C_2H_4 generation is the dimerization of *CO and *CHO toward an intermediate

*CO–CHO (Fig. S24b), which is also the initial step of C2+ products generation. A gentle uphill energy barrier contributes to the considerable multi-carbon product selectivity of the Cl^-_Br^-_SO_4^{2-} mixed electrolyte, which is in agreement with past literature [60,61] and the above-mentioned experiment results.

To assess the influence of different seawater-based anions mixed electrolytes on gas-bubble adsorption/desorption of CO_2 and key gaseous products (*i.e.* CO, CH_4) [62], we tested the adhesive force behavior of CO_2, CO, and CH_4 bubbles on the surface of Cu electrode in the four different anions mixed electrolytes separately (Figs. S34–S36). The Cl^-_Br^-_SO_4^{2-} mixed electrolyte gives a weaker CO_2 adhesive force of 10.1 mg on Cu than others (Fig. S34), which means CO_2 bubbles detached easily from the electrode surface, and considerable mass transfer was obtained. Additionally, weak CO and CH_4 gaseous bubble adhesive force between the electrode and Br^-_SO_4^{2-} electrolyte causes low liquid product selectivity (Fig. S37). This was attributed to the concentration of non-buffer ions (Cl^- and SO_4^{2-}) is low, higher concentration of dissolved CO_2 and a more neutral bulk environment resulted in higher selectivity for several multi-carbon products, especially ethanol, as shown in Fig. S38. Therefore, in comparison, the selectivity of liquid products is slightly higher in this electrolyte.

3.5. The optimization strategy

Given the above findings and analyses, we believe that multi-ions in seawater have the potential for promoting CO_2RR. It was therefore necessary to design and propose an optimization strategy for directly conducting CO_2RR in seawater. Since the mass transfer disadvantage caused by a high concentration of ions is dominant in seawater after removing Ca^{2+} and Mg^{2+}, we performed the optimization of concentration. The electrolyte (without Ca^{2+} and Mg^{2+}) was diluted by factors of 0.5, 0.8, 1, 1.25, and 2–fold, respectively (Fig. 5a). The CO_2RR performance shows that the 1–fold diluted solution (Table S1, marked optimized 2) has the lowest selectivity to hydrogen (*c.a.* 39 %) and current density (9 mA cm^{-2}) at −1.1 V *vs.* RHE. Therefore, we selected the 1–fold dilution on concentration optimization for CO_2RR. After optimization, the yield of H_2, CO, methane and methanol was 0.176 μM/s/cm^2, 0.000146 μM/s/cm^2, 0.00802 μM/s/cm^2, and 0.0128 μM/s/cm^2, separately, at an applied potential of −1.15 V *vs.* RHE (Fig. S39). Potentials at −10 mA/cm^2 in the optimized electrolyte dropped by −56 mV compared to simulated seawater before optimization (Fig. S40). Also, the decreased adhesive force behavior of CO_2 bubbles (Fig. S41) was beneficial to the diffusion and mass transfer of CO_2 after optimization.

These findings on the Cu plate are appropriate and necessary for mechanistic studies. When it comes to practical application, the unbreakable high overpotentials of bulk aqueous H-cell (almost less than 100 mA/cm^{-2}) would be the insurmountable barriers [63,64]. Given the outstanding performance on mass transfer and high energy density conversion [36,64–66]. we thereafter carried out the CO_2RR in this optimized seawater by using a GDE cell. The Cu NPs (nanoparticles) dropped on carbon paper (Cu@CC) were used as the cathode (Figs. S42–S43) and a NiFe LDH (layered double hydroxide) was prepared for anode (Figs. S44–S45) [67]. Compared with the Pt anode, the cell voltage dropped from 4.3 V to 2.3 V at 20 mA/cm^2 by using NiFe LDH in the optimized electrolyte (Fig. S46). As such, the current density of GDE cell was improved 2.3 times at −1.1 V *vs.* RHE, while the selectivity of oxygenates was boosted for *c.a.* 23 times (Fig. 5b). The HER was suppressed by close to 30 % (Fig. S47). Therefore, the barrier of ions concentration in seawater was alleviated and the catalysts overpotential is efficiently reduced.

3.6. Solar-driven CO_2RR with optimized seawater

For practical and carbon-free applications, we connected the GDE cell with a commercial Si solar cell to operate the CO_2RR in the previously optimized seawater under directly natural sunlight (Figs. 6a and S48). Within, the NiFe LDH and Cu@CC served as anode and cathode, separately, and an anion exchange membrane was placed between the cathodic and anodic chambers. As-prepared optimized seawater after CO_2 saturated was pumped into chambers and 15 sccm CO_2 was bubbled continuously during the test. Eight series-connected Si cells (LONGi Co., Ltd.) with total illumination areas of 12 cm^2 were used for operating CO_2RR at −20 mA/cm^2. An optical bracket with an auto-tracking module was used to assemble PV cell to ensure that sunlight irradiated the surface of the panel vertically. A PC–2–T1 solar radiation monitoring system was used to measure the intensity of sunlight irradiated to the ground (Xi'an, China. 34°14′ N, 108°59′ E, 420 m Elevation, the air temperature was 28–35 °C, Cloudy, in Table S5), and the P was recorded every 20 min

As shown in Fig. 6b, at 1:00 PM on the first day (P = 532 W m^{-2}), the Si cell (without electrochemical electrolyzer) achieved an open circuit

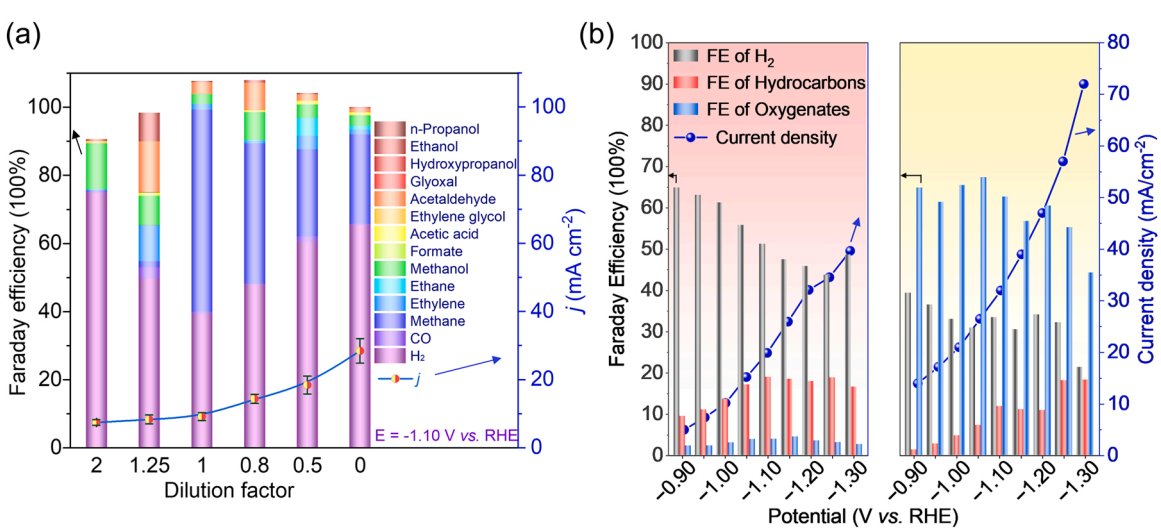

Fig. 5. An optimization strategy on the concentration of ions in seawater and the CO_2RR performance on Cu@CC//NiFe LDH GDE cell. (a) The optimization results in different dilution factors of the seawater with Ca^{2+} and Mg^{2+} removed. The solid line with a red dot indicates the current density change trend at different concentrations. Error bars represent the mean ± standard deviation of at least 3 individual experiments. (b) Comparison of CO_2RR performance at different applied potentials before and after system optimization. The right panel depicts the CO_2RR data from Cu//Pt in H-cell, while the right panel depicts that in a Cu@CC//NiFe LDH GDE cell.

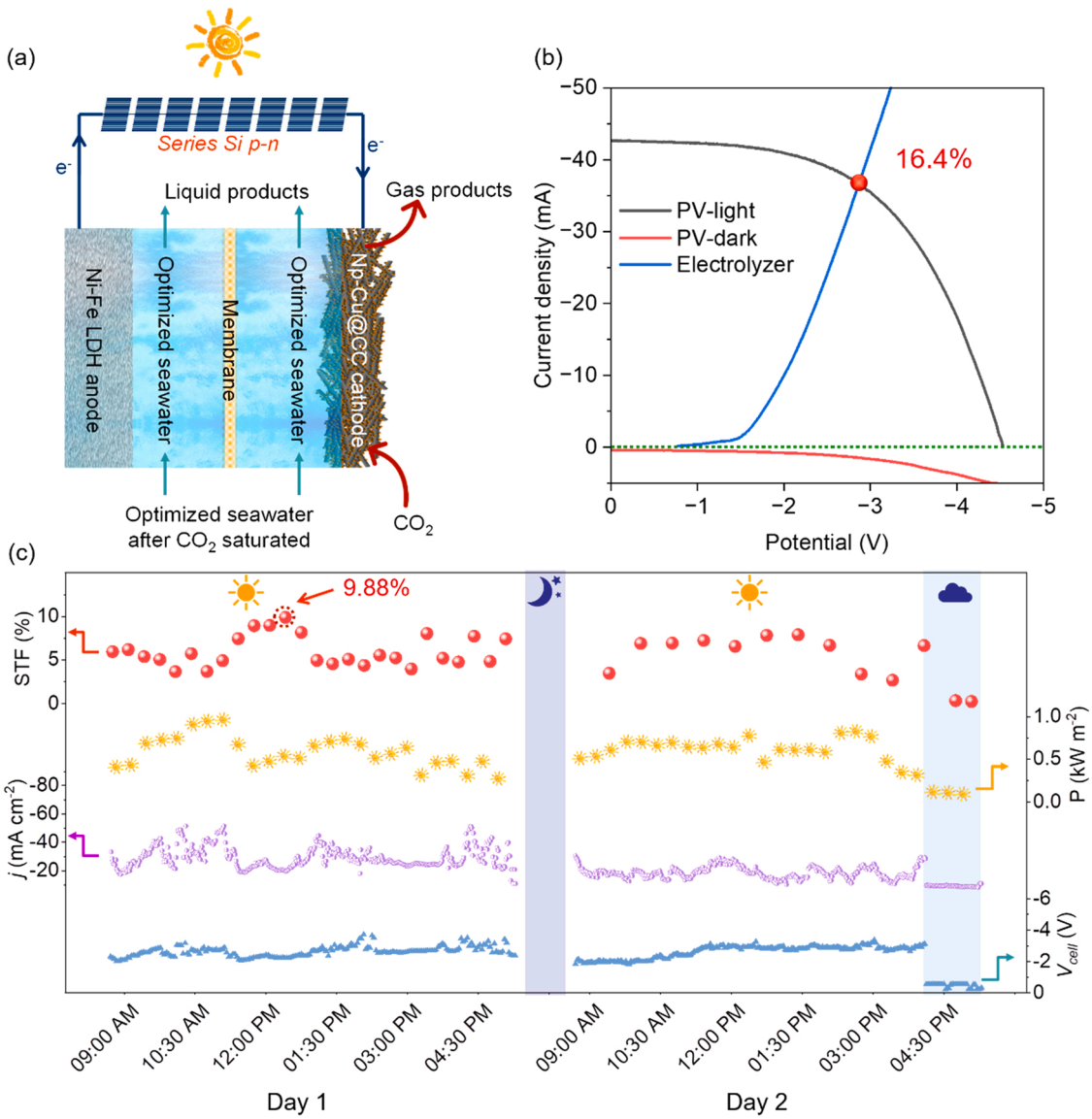

Fig. 6. CO_2RR in the optimized seawater-based electrolyte under a Si PV–cell combined with the Cu@CC//NiFe LDH GDE cell. (a) Schematic illustration of PV-GDE CO_2RR system. (b) The current density–potential (*j–V*) curve of Si solar cells under dark and real sunlight with 532 W/m^2 illuminations, and the electrochemical CO_2RR under a Cu@CC//NiFe LDH GDE cell. (c) Irradiation intensity, STF efficiency, current density, and cell voltage curves over a two-daylight duration.

voltage of −4.52 V, a short circuit current density of *ca.* –42.5 ± 0.1 mA/cm^2. After coupling the Si solar cell with Cu@CC//NiFe LDH GDE electrolyzer, the intersection of the *j–V* curves measured independently by the solar cell and the electrochemical cell indicates that the operating current and voltage of the integrated solar-driven CO_2RR can be set at –36 ± 0.1 mA/cm^2 and 2.91 V, corresponding to a calculated η_{pv} was 16.4 %. Over two-daylights' outdoor test (Fig. 6c), the output voltage of the Si–cell was around −2.6 V for most of the period, while the photocurrent density changed over time. After 4 p.m. on the second day, the electrochemical signal and light irradiance dropped to very low levels as the weather turned cloudy. The photovoltaic electrolysis reaction is almost terminated. At 1:10 PM on the first day, the measured STF efficiency reached 9.88 % (corresponding to −33.28 mA/cm^2, P = 528 W m^{-2}), of which the efficiency of solar to carbon-based fuels is up to 6.15 %. Correspondingly, the FE of CO_2RR products could be close to 40 % (Fig. S49), which was pioneered in several seawater-based works (Table S6).

4. Conclusion

In summary, we investigated CO_2RR in seawater-based electrolytes on Cu electrodes in terms of ion species, concentration, and multi-ions mixtures. CO_2RR in natural seawater was blocked by the precipitation generated from Ca^{2+} and Mg^{2+} within several hours at about –5 mA/cm^2. After removing Ca^{2+} and Mg^{2+}, current hindrance to the reaction is removed, but the performance of CO_2RR is still affected by the ion species and concentration. Larger radius K^+ with vaster buffering capacity is preferred to produce hydrocarbons than Na^+. Cl^- and Br^- in electrolyte had better CO_2RR performance due to stronger solvation ability, stronger specific adsorption, and lower energy barrier for *COOH formation. The suitable Na^+ or Cl^- electrolyte concentration range for CO_2RR was 0.05 – 0.3 M, which was attributed to adequate mass transfer effect and dielectric properties. We proposed a hierarchical application mechanism in multi-ions mixed electrolytes based on seawater. Roughening and reconstruction of electrode surface appeared where Cl^- and Br^- existed, even the Cu(0) on the copper electrode had been partially oxidized for generating activated Cu sites in the Cl^-_Br^-_SO_4^{2-} system to accelerate the CO_2RR. Na^+_K^+ cations–coupling

had a feasible buffer capacity for regulating the interfacial pH. The SO_4^{2-} could reduce polarization loss of bulk electrolyte to lower the overpotential. Besides, a lower energy barrier in the dualization of *CO and *CHO caused a considerable C2+ selectivity in the Cl^-_Br^-_SO_4^{2-} mixed system. After concertation optimization, we performed CO_2RR on the GDE electrolyzer with Cu@CC cathode coupled NiFe LDH anode. The current density and oxygenates' selectivity were improved by ~2.3 times and ~23 times, respectively. Finally, we conducted a Si PV-driven electrolysis of CO_2RR in the optimized seawater by using a GDE electrolyzer, and a 9.88 % solar-to-fuel efficiency (6.15 % solar-to-carbon-based fuels) was obtained at 1:10 PM (Xi'an, China. 34°14′ N, 108°59′ E, 420 m Elevation, 31 °C) corresponding to a current density of −33.28 mA/cm^2.

CRediT authorship contribution statement

Shengjie Bai: Conceptualization, Investigation, Validation, Writing – original draft, Visualization, Writing – review & editing. **Mengmeng Song:** Formal analysis, Methodology, Writing – review & editing. **Tengfei Ma:** Investigation, Resources, Writing – review & editing. **Feng Wang:** Resources, Writing – review & editing. **Ya Liu:** Conceptualization, Project administration, Writing – review & editing. **Liejin Guo:** Supervision, Funding acquisition.

Declaration of Competing Interest

The authors declare that they have no known competing financial interests or personal relationships that could have appeared to influence the work reported in this paper.

Data availability

Data will be made available on request.

Acknowledgements

This work is supported by the Basic Science Center Program for Ordered Energy Conversion of the National Natural Science Foundation of China (No. 51888103) and the Fundamental Research Funds for the Central Universities.

Appendix A. Supporting information

Supplementary data associated with this article can be found in the online version at doi:10.1016/j.apcatb.2022.122166.

References

[1] B. Endrődi, A. Samu, E. Kecsenovity, T. Halmágyi, D. Sebők, C. Janáky, Operando cathode activation with alkali metal cations for high current density operation of water-fed zero-gap carbon dioxide electrolysers, Nat. Energy 6 (2021) 439–448.
[2] M. Li, B. Hua, L.-C. Wang, J.D. Sugar, W. Wu, Y. Ding, J. Li, D. Ding, Switching of metal–oxygen hybridization for selective CO_2 electrohydrogenation under mild temperature and pressure, Nat. Catal. 4 (2021) 274–283.
[3] Z. Huang, R.G. Grim, J.A. Schaidle, L. Tao, The economic outlook for converting CO_2 and electrons to molecules, Energy Environ. Sci. 14 (2021) 3664–3678.
[4] D. Wakerley, S. Lamaison, J. Wicks, A. Clemens, J. Feaster, D. Corral, S.A. Jaffer, A. Sarkar, M. Fontecave, E.B. Duoss, S. Baker, E.H. Sargent, T.F. Jaramillo, C. Hahn, Gas diffusion electrodes, reactor designs and key metrics of low-temperature CO_2 electrolysers, Nat. Energy 7 (2022) 130–143.
[5] S. Bai, H. Qiu, M. Song, G. He, F. Wang, Y. Liu, L. Guo, Porous fixed-bed photoreactor for boosting C–C coupling in photocatalytic CO_2 reduction, eScience 2 (2022) 428–437.
[6] Y. Liu, F. Wang, Z. Jiao, S. Bai, H. Qiu, L. Guo, Photochemical systems for solar-to-fuel production, Electrochem. Energy Rev. 5 (2022) 5.
[7] J.N. Hausmann, R. Schlögl, P.W. Menezes, M. Driess, Is direct seawater splitting economically meaningful? Energy Environ. Sci. 14 (2021) 3679–3685.
[8] M. Jiskra, L.E. Heimburger-Boavida, M.M. Desgranges, M.V. Petrova, A. Dufour, B. Ferreira-Araujo, J. Masbou, J. Chmeleff, M. Thyssen, D. Point, J.E. Sonke, Mercury stable isotopes constrain atmospheric sources to the ocean, Nature 597 (2021) 678–682.
[9] P. Farras, P. Strasser, A.J. Cowan, Water electrolysis: direct from the sea or not to be? Joule 5 (2021) 1921–1923.
[10] B.E. Logan, L. Shi, R. Rossi, Enabling the use of seawater for hydrogen gas production in water electrolyzers, Joule 5 (2021) 760–762.
[11] M. Gao, C.K. Peh, L. Zhu, G. Yilmaz, G.W. Ho, Photothermal catalytic gel featuring spectral and thermal management for parallel freshwater and hydrogen production, Adv. Energy Mater. 10 (2020) 2000925.
[12] A. Gopakumar, P. Ren, J. Chen, B.V. Manzolli Rodrigues, H.Y. Vincent Ching, A. Jaworski, S.V. Doorslaer, A. Rokicińska, P. Kuśtrowski, G. Barcaro, S. Monti, A. Slabon, S. Das, Lignin-supported heterogeneous photocatalyst for the direct generation of H_2O_2 from seawater, J. Am. Chem. Soc. 144 (2022) 2603–2613.
[13] H. Jin, X. Wang, C. Tang, A. Vasileff, L. Li, A. Slattery, S.-Z. Qiao, Stable and highly efficient hydrogen evolution from seawater enabled by an unsaturated nickel surface nitride, Adv. Mater. 33 (2021) 2007508.
[14] S.S. Veroneau, D.G. Nocera, Continuous electrochemical water splitting from natural water sources via forward osmosis, Proc. Natl. Acad. Sci. USA 118 (2021), e2024855118.
[15] N. Kazuya, O. Takuya, T. Chiaki, F. Akira, E. Yasuaki, High-yield electrochemical production of formaldehyde from CO_2 and seawater, Angew. Chem., Int. Ed. 126 (2014) 890–893.
[16] C.-Y. Lee, G.G. Wallace, CO_2 electrolysis in seawater: calcification effect and a hybrid self-powered concept, J. Mater. Chem. A 6 (2018) 23301–23307.
[17] I.A. Digdaya, I. Sullivan, M. Lin, L. Han, W.-H. Cheng, H.A. Atwater, C. Xiang, A direct coupled electrochemical system for capture and conversion of CO_2 from oceanwater, Nat. Commun. 11 (2020) 4412.
[18] A. Murata, Y. Hori, Product selectivity affected by cationic species in electrochemical reduction of CO_2 and CO at a Cu electrode, B Chem. Soc. Jpn. 64 (1991) 123–127.
[19] D. Gao, F. Scholten, B.R. Cuenya, Improved CO_2 electroreduction performance on plasma-activated Cu catalysts via electrolyte design: Halide effect, ACS Catal. 7 (2017) 5112–5120.
[20] M.M. Sartin, Z. Yu, W. Chen, F. He, Z. Sun, Y. Chen, W. Huang, The effect of particle shape and electrolyte cation on CO adsorption to copper oxide nanoparticle electrocatalysts, J. Phys. Chem. C 122 (2018) 26489–26498.
[21] M.R. Singh, Y. Kwon, Y. Lum, J.W. Ager, A.T. Bell, Hydrolysis of electrolyte cations enhances the electrochemical reduction of CO_2 over Ag and Cu, J. Am. Chem. Soc. 138 (2016) 13006–13012.
[22] M.R. Singh, E.L. Clark, A.T. Bell, Effects of electrolyte, catalyst, and membrane composition and operating conditions on the performance of solar-driven electrochemical reduction of carbon dioxide, Phys. Chem. Chem. Phys. 17 (2015) 18924–18936.
[23] S. Verma, B. Kim, H.-R.M. Jhong, S. Ma, P.J.A. Kenis, A. Gross-Margin, Model for defining technoeconomic benchmarks in the electroreduction of CO_2, ChemSusChem 9 (2016) 1972–1979.
[24] W. Zheng, Y. Liu, S. Bai, H. Qiu, J. Wu, Y. Chen, Simulation study reveals the role of hydrogen spillover in pH- and potential-dependent hydrogen evolution over the NiCu bimetal catalyst, J. Phys. Chem. C 126 (2022) 13182–13190.
[25] M. Song, Z. Jiao, W. Jing, Y. Liu, L. Guo, Revealing the nature of C–C coupling sites on a Cu surface for CO_2 reduction, J. Phys. Chem. Lett. 13 (2022) 4434–4440.
[26] X. Lu, C. Zhao, Electrodeposition of hierarchically structured three-dimensional nickel–iron electrodes for efficient oxygen evolution at high current densities, Nat. Commun. 6 (2015) 6616.
[27] S. Fukuzumi, Y.M. Lee, W. Nam, Fuel production from seawater and fuel cells using seawater, ChemSusChem 10 (2017) 4264–4276.
[28] S. Ringe, E.L. Clark, J. Resasco, A. Walton, B. Seger, A.T. Bell, K. Chan, Understanding cation effects in electrochemical CO_2 reduction, Energy Environ. Sci. 12 (2019) 3001–3014.
[29] O. Ayemoba, A. Cuesta, Spectroscopic evidence of size-dependent buffering of interfacial pH by cation hydrolysis during CO_2 electroreduction, ACS Appl. Mater. Interfaes 9 (2017) 27377–27382.
[30] A. Xu, N. Govindarajan, G. Kastlunger, S. Vijay, K. Chan, Theories for electrolyte effects in CO_2 electroreduction, Acc. Chem. Res. 55 (2022) 495–503.
[31] O. Magnussen, Ordered anion adlayers on metal electrode surfaces, Chem. Rev. 102 (2002) 679–726.
[32] D. Tripkovic, D. Strmcnik, D. Van Der Vliet, V. Stamenkovic, N. Markovic, The role of anions in surface electrochemistry, Faraday Discuss. 140 (2009) 25–40.
[33] B.W. Deng, M. Huang, X.L. Zhao, S.Y. Mou, F. Dong, Interfacial electrolyte effects on electrocatalytic CO_2 reduction, ACS Catal. 12 (2022) 331–362.
[34] Y.Y. Cheng, P.F. Hou, X.P. Wang, P. Kang, CO_2 electrolysis system under industrially relevant conditions, Acc. Chem. Res. 55 (2022) 231–240.
[35] K. Krause, J.K. Lee, C. Lee, H.W. Shafaque, P.J. Kim, K.F. Fahy, P. Shrestha, J. M. LaManna, E. Baltic, D.L. Jacobson, D.S. Hussey, A. Bazylak, Electrolyte layer gas triggers cathode potential instability in CO_2 electrolyzers, J. Power Sources 520 (2022).
[36] K. Ye, G. Zhang, X.-Y. Ma, C. Deng, X. Huang, C. Yuan, G. Meng, W.-B. Cai, K. Jiang, Resolving local reaction environment toward an optimized CO_2-to-CO conversion performance, Energy Environ. Sci. 15 (2022) 749–759.
[37] J.H. Montoya, C. Shi, K. Chan, J.K. Nørskov, Theoretical insights into a CO dimerization mechanism in CO_2 electroreduction, J. Phys. Chem. Lett. 6 (2015) 2032–2037.
[38] A.M.E. Badawy, T.P. Luxton, R.G. Silva, K.G. Scheckel, M.T. Suidan, T. M. Tolaymat, Impact of environmental conditions (pH, ionic strength, and electrolyte type) on the surface charge and aggregation of silver nanoparticles suspensions, Environ. Sci. Technol. 44 (2010) 1260–1266.
[39] J. Teychené, H.R.-d Balmann, L. Maron, S. Galier, Investigation of ions hydration using molecular modeling, J. Mol. Liq. 294 (2019), 111394.

[40] J.-J. Lv, M. Jouny, W. Luc, W. Zhu, J.-J. Zhu, F. Jiao, A highly porous copper electrocatalyst for carbon dioxide reduction, Adv. Mater. 30 (2018) 1803111.
[41] Y.Y. Birdja, E. Pérez-Gallent, M.C. Figueiredo, A.J. Göttle, F. Calle-Vallejo, M.T. M. Koper, Advances and challenges in understanding the electrocatalytic conversion of carbon dioxide to fuels, Nat. Energy 4 (2019) 732–745.
[42] T. Burdyny, W.A. Smith, CO_2 reduction on gas-diffusion electrodes and why catalytic performance must be assessed at commercially-relevant conditions, Energy Environ. Sci. 12 (2019) 1442–1453.
[43] M. Dunwell, Q. Lu, J.M. Heyes, J. Rosen, J.G. Chen, Y. Yan, F. Jiao, B. Xu, The central role of bicarbonate in the electrochemical reduction of carbon dioxide on gold, J. Am. Chem. Soc. 139 (2017) 3774–3783.
[44] C. Zhao, Y. Wang, Z. Li, W. Chen, Q. Xu, D. He, D. Xi, Q. Zhang, T. Yuan, Y. Qu, J. Yang, F. Zhou, Z. Yang, X. Wang, J. Wang, J. Luo, Y. Li, H. Duan, Y. Wu, Y. Li, Solid-diffusion synthesis of single-atom catalysts directly from bulk metal for efficient CO_2 reduction, Joule 3 (2019) 584–594.
[45] Y. Hori, R. Takahashi, Y. Yoshinami, A. Murata, Electrochemical reduction of CO at a copper electrode, J. Phys. Chem. B 101 (1997) 7075–7081.
[46] S. Ding, M.J. Hülsey, J. Pérez-Ramírez, N. Yan, Transforming energy with single-atom catalysts, Joule 3 (2019) 2897–2929.
[47] C. Hahn, T.F. Jaramillo, Using microenvironments to control reactivity in CO_2 electrocatalysis, Joule 4 (2020) 292–294.
[48] J. Resasco, Y. Lum, E. Clark, J.Z. Zeledon, A.T. Bell, Effects of anion identity and concentration on electrochemical reduction of CO_2, ChemElectroChem 5 (2018) 1064–1072.
[49] F. Chen, Y. Huang, L. Guo, L. Sun, Y. Wang, H.Y. Yang, Dual-ions electrochemical deionization: a desalination generator, Energy Environ. Sci. 10 (2017) 2081–2089.
[50] T.M. Arruda, B. Shyam, J.M. Ziegelbauer, S. Mukerjee, D.E. Ramaker, Investigation into the competitive and site-specific nature of anion adsorption on Pt using in situ X-ray absorption spectroscopy, J. Phys. Chem. C 112 (2008) 18087–18097.
[51] F.S. Roberts, K.P. Kuhl, A. Nilsson, High selectivity for ethylene from carbon dioxide reduction over copper nanocube electrocatalysts, Angew. Chem., Int. Ed. 54 (2015) 5179–5182.
[52] A. Zolfaghari, B.E. Conway, G. Jerkiewicz, Elucidation of the effects of competitive adsorption of Cl^- and Br^- ions on the initial stages of Pt surface oxidation by means of electrochemical nanogravimetry, Electrochim. Acta 47 (2002) 1173–1187.
[53] S. Narayanaru, J. Chinnaiah, K.L. Phani, F. Scholz, pH dependent CO adsorption and roughness-induced selectivity of CO_2 electroreduction on gold surfaces, Electrochim. Acta 264 (2018) 269–274.
[54] C.W. Li, M.W. Kanan, CO_2 reduction at low overpotential on Cu electrodes resulting from the reduction of thick Cu_2O films, J. Am. Chem. Soc. 134 (2012) 7231–7234.
[55] Z. Chen, T. Wang, B. Liu, D. Cheng, C. Hu, G. Zhang, W. Zhu, H. Wang, Z.-J. Zhao, J. Gong, Grain-boundary-rich copper for efficient solar-driven electrochemical CO_2 reduction to ethylene and ethanol, J. Am. Chem. Soc. 142 (2020) 6878–6883.
[56] M.C. Biesinger, Advanced analysis of copper X-ray photoelectron spectra, Surf. Interface Anal. 49 (2017) 1325–1334.
[57] J. Wang, H.-Y. Tan, Y. Zhu, H. Chu, H.M. Chen, Linking dynamic chemical state of catalysts with product profile of electrocatalytic CO_2 reduction, Angew. Chem. Int. Ed. 133 (2021) 2–16.
[58] D. Mateo, J. Albero, H. Garcia, Photoassisted methanation using Cu_2O nanoparticles supported on graphene as a photocatalyst, Energy Environ. Sci. 10 (2017) 2392–2400.
[59] M. Schreier, P. Gao, M.T. Mayer, J.S. Luo, T. Moehl, M.K. Nazeeruddin, S.D. Tilley, M. Gratzel, Efficient and selective carbon dioxide reduction on low cost protected Cu_2O photocathodes using a molecular catalyst, Energy Environ. Sci. 8 (2015) 855–861.
[60] H. Wang, Z. Liang, M. Tang, G. Chen, Y. Li, W. Chen, D. Lin, Z. Zhang, G. Zhou, J. Li, Z. Lu, K. Chan, T. Tan, Y. Cui, Self-selective catalyst synthesis for CO_2 reduction, Joule 3 (2019) 1927–1936.
[61] T. Cheng, H. Xiao, W.A. Goddard, Full atomistic reaction mechanism with kinetics for CO reduction on Cu(100) from ab initio molecular dynamics free-energy calculations at 298 K, Proc. Natl. Acad. Sci. USA 114 (2017) 1795–1800.
[62] W. Xu, Z. Lu, X. Sun, L. Jiang, X. Duan, Superwetting electrodes for gas-involving electrocatalysis, Acc. Chem. Res 51 (2018) 1590–1598.
[63] M. de Jesus Gálvez-Vázquez, P. Moreno-García, H. Xu, Y. Hou, H. Hu, I.Z. Montiel, A.V. Rudnev, S. Alinejad, V. Grozovski, B.J. Wiley, M. Arenz, P. Broekmann, Environment matters: CO_2RR electrocatalyst performance testing in a gas-fed zero-gap electrolyzer, ACS Catal. 10 (2020) 13096–13108.
[64] W.-H. Cheng, M.H. Richter, I. Sullivan, D.M. Larson, C. Xiang, B.S. Brunschwig, H. A. Atwater, CO_2 reduction to CO with 19% efficiency in a solar-driven gas diffusion electrode flow cell under outdoor solar illumination, ACS Energy Lett. 5 (2020) 470–476.
[65] H. Rabiee, L. Ge, X. Zhang, S. Hu, M. Li, Z. Yuan, Gas diffusion electrodes (GDEs) for electrochemical reduction of carbon dioxide, carbon monoxide, and dinitrogen to value-added products: a review, Energy Environ. Sci. 14 (2021) 1959–2008.
[66] S. Popović, M. Smiljanić, P. Jovanovič, J. Vavra, R. Buonsanti, N. Hodnik, Stability and degradation mechanisms of copper-based catalysts for electrochemical CO_2 reduction, Angew. Chem., Int. Ed. 59 (2020) 14736–14746.
[67] Y. Kuang, M.J. Kenney, Y. Meng, W.-H. Hung, Y. Liu, J.E. Huang, R. Prasanna, P. Li, Y. Li, L. Wang, Solar-driven, highly sustained splitting of seawater into hydrogen and oxygen fuels, Proc. Natl. Acad. Sci. USA 116 (2019) 6624–6629.